

Splitting and recombination of bright-solitary-matter waves

Oliver J. Wales ¹, Ana Rakonjac ¹, Thomas P. Billam², John L. Helm³, Simon A. Gardiner¹ & Simon L. Cornish ¹✉

Atomic Bose–Einstein condensates confined in quasi-1D waveguides can support bright-solitary-matter waves when interatomic interactions are sufficiently attractive to cancel dispersion. Such solitary-matter waves are excellent candidates for highly sensitive interferometers, as their non-dispersive nature allows them to acquire phase shifts for longer times than conventional matter-wave interferometers. In this work, we demonstrate experimentally the splitting and recombination of a bright-solitary-matter wave on a narrow repulsive barrier, realizing the fundamental components of an interferometer. We show that for a sufficiently narrow barrier, interference-mediated recombination can dominate over velocity-filtering effects. Our theoretical analysis shows that interference-mediated recombination is extremely sensitive to the barrier position, predicting strong oscillations in the interferometer output as the barrier position is adjusted over just a few micrometres. These results highlight the potential of soliton interferometry, while putting tight constraints on the barrier stability needed in future experimental implementations.

¹Joint Quantum Centre (JQC) Durham–Newcastle, Department of Physics, Durham University, South Road, Durham DH1 3LE, UK. ²Joint Quantum Centre (JQC) Durham–Newcastle, School of Mathematics, Statistics and Physics, Newcastle University, Newcastle upon Tyne NE1 7RU, UK. ³Dodd-Walls Centre for Photonic and Quantum Technologies, Department of Physics, University of Otago, 730 Cumberland Street, Dunedin 9016, New Zealand. ✉email: s.l.cornish@durham.ac.uk

Bright-solitary waves, referred to as solitons in this work, are wavepackets that propagate in a quasi-one-dimensional (1D) geometry without dispersion, owing to a self-focussing nonlinearity. They are of fundamental interest in a broad range of settings due to their ubiquity in nonlinear systems, which occur prolifically in nature^{1,2}. In Bose–Einstein condensates (BECs), the nonlinearity is provided by interatomic interactions governed by the *s*-wave scattering length, which can be tuned using a magnetic Feshbach resonance³. To date, bright solitons in BECs of ⁷Li, ⁸⁵Rb, ³⁹K and ¹³³Cs have been experimentally demonstrated^{4–10}. Understanding and probing the coherent phase carried by matter-wave solitons is an area of particular relevance, both because it is important in determining the stability of soliton–soliton collisions^{10–14} and because there is a great interest in using solitons for atom interferometry^{15–22}.

Matter-wave interferometers have emerged as a means of achieving unprecedented sensitivity in interferometric measurements^{23–26}. However, they have typically been limited by either interatomic collisions or dispersion of the atomic wavepackets, which cause dephasing and a reduced signal to noise, respectively²⁷. Previous works have successfully reduced the impact of interatomic collisions through the control of interatomic interactions^{28,29}, or by generating squeezed states^{30,31}. However, dispersion remains a limitation. A soliton-based interferometer has the potential to overcome dispersion, allowing for much longer phase-accumulation times, albeit for an increased quantum noise³². To date, only one experiment has demonstrated interferometry with a soliton⁸, in which Bragg pulses were used for splitting and recombination. However, interferometer times were too low for the non-dispersive property of solitons to have a significant impact.

Narrow repulsive barriers have been proposed as atomic beam splitters for soliton-based interferometers^{15–22,33,34}. Within the framework of the Gross–Pitaevskii equation (GPE), a soliton incident on such a barrier is split cleanly into transmitted and reflected daughter solitons, provided the incident velocity is sufficiently fast that the effects of interatomic interactions can be neglected during the splitting³⁵. When these daughter solitons are subsequently made to spatio-temporally overlap at the barrier, total or partial interference-mediated recombination occurs, depending on their relative phase²¹. This phase-sensitive splitting and recombination forms the basis of the interferometer.

In this work, we demonstrate the splitting and recombination of a soliton on such a repulsive Gaussian barrier. We show that for a barrier much wider than the soliton width, velocity-filtering effects dominate, precluding applications to interferometry. In this case, we observe that the majority of the population consistently appears on the original left side of the barrier after the second barrier interaction. However, for a barrier width approaching the soliton length scale, interference becomes significant, despite velocity-filtering effects still being present and measurable. In this case, the majority of the population can appear on either side of the barrier following recombination, depending on the relative phase and spatio-temporal overlap of the daughter solitons. We investigate, both experimentally and theoretically, the sensitivity to the barrier position of the interference-mediated recombination. Theoretically, we predict strong oscillations in the interferometer output as the barrier position is adjusted over just a few micrometres. Experimentally, we observe large fluctuations in the interferometer output, consistent with interference-mediated recombination in the presence of known shot-to-shot fluctuations in the barrier position. These results highlight the potential of soliton interferometry, while putting tight constraints on the barrier stability needed in future experimental implementations of soliton interferometry.

Results

Controllable splitting. We form a soliton of ~ 2500 ⁸⁵Rb atoms in a quasi-1D waveguide with a radial trapping frequency of 40 Hz, following procedures described elsewhere^{7,36–38}. An additional harmonic magnetic potential produces axial trapping frequencies of up to 1.5 Hz along the waveguide. The soliton undergoes centre of mass oscillations of controllable amplitude in this potential. Measurements are taken using a destructive absorption imaging technique (see Methods); throughout this paper, each image shows the measured optical depth and represents an individual run of the experiment. We have observed soliton lifetimes of longer than 20 s in this potential.

To split a soliton, we use a repulsive Gaussian barrier formed by a blue-detuned highly elliptical laser beam, which is focussed down to bisect the waveguide. We investigate two barrier widths: a “wide” barrier and a “narrow” barrier, with experimentally determined waists ($1/e^2$ radii) of $10.6^{+0.5}_{-0.1}$ μm and 3.6 ± 0.4 μm , respectively (see Methods). Here, the width of the barrier should be compared with the width of the sech-squared soliton wavefunction, $\ell_s = \hbar/(2m\omega_r|a_s|N)$, where ω_r is the radial trap frequency, a_s is the scattering length and N is the atom number. Typically, $\ell_s \sim 1.1$ μm in our experiments, corresponding to an equivalent $1/e^2$ Gaussian width of ~ 1.8 μm . Upon reaching the barrier, the soliton is either reflected, transmitted, or split into two daughter solitons (Fig. 1a). The barrier height and therefore the transmission through the barrier is tuned experimentally by varying the total barrier power (Fig. 1b, c). This enables us to reliably achieve 50:50 splitting of the soliton (Fig. 1d).

Our experiment operates in the regime of fast collisions, such that the total centre of mass kinetic energy of the soliton dominates over the interaction energy of the soliton. In this regime, splitting is possible and mean-field theory is relevant²⁰. This is different from the regime of slow collisions, where splitting is suppressed and quantum superpositions of the entire soliton are predicted^{39,40}. For fast collisions, the nature of the splitting mechanism depends critically on the barrier width. In the limit of a δ -function barrier, quantum tunnelling dominates and the area of the barrier potential determines the transmission probability²⁰. However, for barriers wider than the soliton width, the transmission probability instead depends primarily on the incident soliton’s centre of mass kinetic energy per atom relative to the barrier height. In this case, the transmission probability is well-approximated by the analytic result for a sech-squared potential⁴¹ (see Methods), which becomes a step function in the classical limit of an infinitely wide barrier.

We investigate the nature of the splitting by varying the barrier power to determine the condition for 50 : 50 splitting and then comparing the calculated height of the barrier with the kinetic energy per atom in the incident soliton (see Fig. 1c). For the wide barrier, quasi-1D GPE simulations yield a transmission of 0.5 when the barrier height is only 1% higher than the kinetic energy per atom of the soliton at the barrier, implying that the splitting mechanism is particle-like, with almost no quantum tunnelling. However, equivalent simulations for the narrow barrier yield a barrier height that is 11% higher than the kinetic energy per atom, indicating that quantum tunnelling plays a small role in this case. Experimentally, we measure a transmission of 0.5 when the barrier height is $11 \pm 2^{+2}_{-5}$ % and $35 \pm 3 \pm 18$ % higher than the soliton kinetic energy per atom at the barrier, for the wide and narrow barriers respectively. Here, the first error is statistical and the second reflects the systematic uncertainty in the barrier width. Our observations are broadly consistent with the theoretical expectation, but a precise comparison is precluded by the uncertainty in the barrier widths (see Methods).

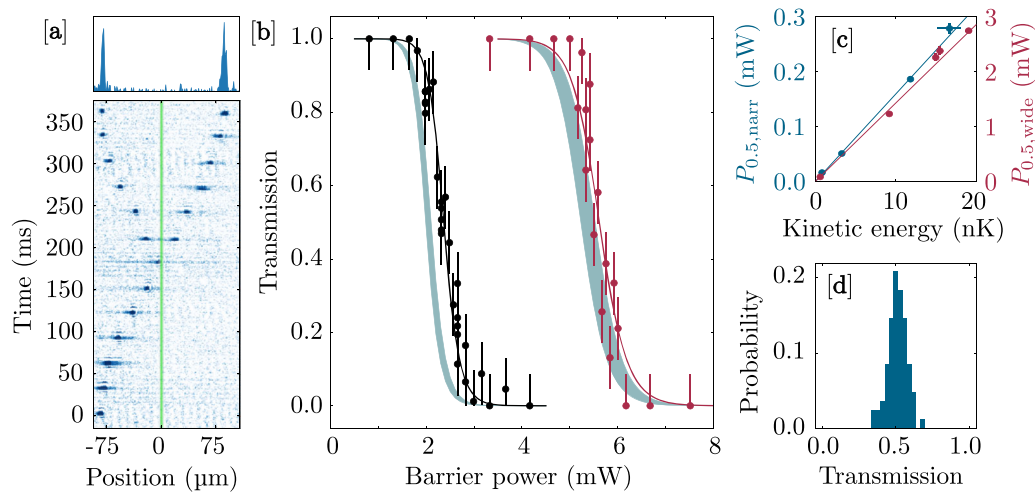


Fig. 1 Controllable splitting of a soliton into two daughter solitons by a repulsive Gaussian barrier. **a** An example sequence of a soliton being split by the narrow barrier into two solitons of approximately equal atom number. The blue shaded region in the upper panel shows the signal obtained by integrating across the final image in the sequence. **b** The transmission of a soliton with a kinetic energy per atom of $E_k/k_B = 15.5 \pm 0.3$ nK (black) and $E_k/k_B = 41 \pm 1$ nK (red) through the wide barrier, as the barrier power is varied. The error bars are estimated from the distribution of repeated transmission measurements when the barrier is set to give equal splitting. The solid lines show the results of quasi-1D Gross-Pitaevskii equation (GPE) simulations using experimental parameters but with the barrier width extracted from a fit to the data, yielding values $w_z = 11.28 \pm 0.06$ μm and $w_z = 12.51 \pm 0.09$ μm , respectively. The grey shaded regions show quasi-1D GPE results with no fitted parameters and the extent of the region reflects the measured uncertainty in barrier width. **c** The barrier power required to achieve a transmission of 0.5 for both the narrow (blue) and wide (red) barriers. The values and uncertainties for the powers and kinetic energies are taken from fits to transmission curves (as in **b**) and trajectories of a soliton oscillating in the same harmonic potential without the barrier respectively. The straight lines are least-squares fits to the experimental data constrained to pass through the origin. The histogram in **d** shows the shot-to-shot variation in transmission for the narrow barrier, for a range of kinetic energies and barrier powers set to give an average transmission of 0.5. This histogram has a SD of 0.064. An equivalent histogram for the wide barrier has a SD of 0.085, which is represented in **b** by the vertical error bars.

Interestingly, the steep energy dependence of the measured transmission functions produces a velocity-filtering effect, whereby the transmitted soliton always has a higher centre of mass kinetic energy than the reflected soliton^{18,22,33}. As a result, the transmitted soliton has a larger oscillation amplitude than the reflected soliton, which we directly observe in the trajectories of the daughter solitons (see Supplementary Fig. 1).

To quantify the reproducibility of the splitting, we take repeated measurements of the final populations for barrier powers calibrated to give an average transmission of 0.5 by fitting to transmission curves similar to those shown in Fig. 1b. The results for the narrow barrier are shown in the histogram in Fig. 1d, which is compiled from datasets across a range of kinetic energies and barrier powers. The observed SD of the histogram is 0.064. From the dependencies in Fig. 1b, c, the measured fluctuations in the barrier power and barrier position are expected to produce shot-to-shot variations in transmission of <0.005 and 0.02, respectively. We conclude that the observed variation is dominated by noise in the absorption imaging measurement of the atom number. This would correspond to $\sim 12\%$ (or ~ 150 atoms) noise for a typical soliton of 2500 atoms. We note that this degree of uncertainty accords with observed inconsistencies between number measurements of Rb and Cs atoms produced from the dissociation of RbCs molecules where we know, a priori, that the number of each species is exactly the same⁴².

Recombination. Interference-mediated recombination occurs when the two daughter solitons return to the barrier and spatio-temporally overlap. Following this second barrier interaction, the resultant populations on each side of the barrier are determined by the relative phase between the daughter solitons—the basis for soliton interferometry (see Fig. 2). It is important to note that the barrier is essential for interference-mediated recombination through its breaking of the system's integrability; in the absence

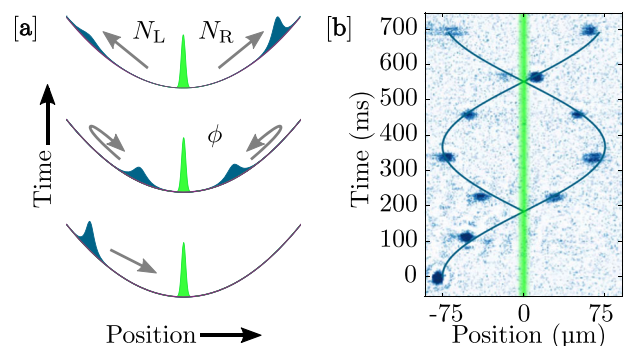


Fig. 2 Soliton interferometry using a repulsive Gaussian barrier as a beam splitter. **a** The initial soliton (blue) propagates in a weak harmonic potential and is split into two daughter solitons by the barrier (green). The daughter solitons oscillate in the potential and return to the barrier, where they interfere, with resultant population fractions on the left and right (N_L and N_R , respectively) determined by their phase difference (ϕ). **b** The experimental implementation of the soliton interferometry scheme, showing a composite image of ^{85}Rb solitons propagating along the weak direction of a quasi-1D optical waveguide for seven different run times. The solid blue lines show the trajectories of the solitons and the green line shows the location of the barrier.

of the barrier, the two daughter solitons simply pass through one another, because the system is close to integrable (see Supplementary Fig. 2).

The splitting process imposes a phase difference between the daughter solitons, which in general depends on the barrier width, the nonlinearity and the soliton velocity. In the limit of a δ -function barrier, theoretical studies²¹ indicate that this phase difference tends to $\pi/2$, and in our quasi-1D GPE simulations, we observe a phase difference close to this value. Under ideal

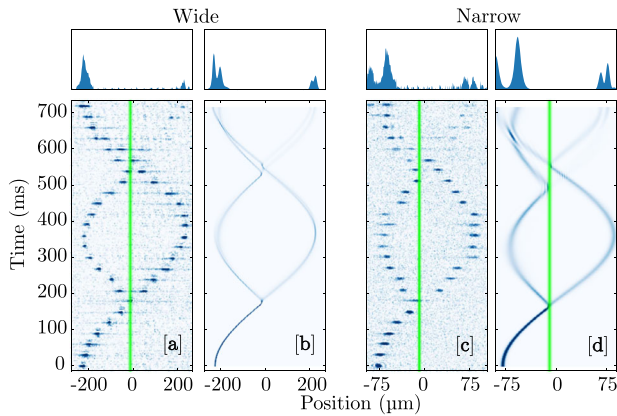


Fig. 3 Trajectories of a soliton with an offset barrier. The soliton undergoes centre of mass oscillations and interacts twice with a barrier that is offset $10\ \mu\text{m}$ from the centre of the harmonic potential. **a, b** The results for the wide barrier where the soliton kinetic energy per atom at the barrier is $E_k/k_B = 19.0 \pm 0.5\ \text{nK}$. **a** The experimental image sequence, with the upper panel displaying the signal obtained by integrating across the final image. **b** The results of quasi-1D Gross-Pitaevskii equation (GPE) simulations, with the upper panel displaying the convolution of the final 1D density and the resolution of the imaging system. The barrier is indicated by the green line and the barrier power is held constant throughout each sequence to give a transmission of 0.5 at the first barrier interaction. **c, d** Similar results for the narrow barrier where the soliton kinetic energy per atom at the barrier is $E_k/k_B = 2.5 \pm 0.4\ \text{nK}$.

conditions, this phase difference is maintained until recombination. For a δ -function barrier, we would then achieve completely constructive (destructive) interference on the right (left) of the barrier, resulting in a fully recombined soliton appearing on the right. However, velocity filtering confounds this ideal outcome. If we remove the effects of interference and consider velocity filtering alone, the reflected (transmitted) daughter soliton is always primarily reflected from (transmitted through) the barrier at the second barrier interaction, resulting in a single wavepacket appearing on the left. This should be considered a merging of the two daughter solitons, rather than true recombination, as it is mediated by velocity filtering and not interference.

To isolate and expose the effects of velocity filtering experimentally, the barrier is offset from the centre of the harmonic potential, preventing the daughter solitons from spatio-temporally overlapping during the second barrier interaction. This removes any possibility of interference. We observe that the population appears almost entirely on the left after the second barrier interaction for both the wide barrier (Fig. 3a, b) and the narrow barrier (Fig. 3c, d). This is consistent with strong velocity filtering. In reality, neither complete interference nor total velocity filtering can be achieved, as it is impossible to realize a δ -function barrier and interactions preclude total velocity filtering (see Methods).

To study interference-mediated recombination, the barrier is aligned with the centre of the harmonic potential to ensure maximal spatio-temporal overlap of the daughter solitons with the barrier. For the wide barrier, we observe that, despite a small increase in population on the right compared with the offset case, the majority of the population still appears on the left after the second barrier interaction (Fig. 4a, b). This indicates that velocity filtering dominates the recombination process for the wide barrier. The outcome for the narrow barrier is markedly different, as shown in Fig. 4c, d. In this case, we can clearly see that the majority of the population is able to finish on the right, which can only be explained by interference-mediated recombination. This

occurs despite the presence of measurable velocity filtering, as highlighted in Fig. 3c, d (see also Supplementary Fig. 1). In practice, the extreme sensitivity of interference-mediated recombination to the experimental parameters leads to large shot-to-shot fluctuations in the final populations on the left and right. This can be seen across the final five images in Fig. 4c; the absence of population on the right in the fourth image from the end of the sequence is real. We show below that the large shot-to-shot population fluctuations at the output of the interferometer can result from small variations in the position of the axial harmonic potential with respect to the barrier.

We explore the dependence of interference-mediated recombination on the offset of the narrow barrier in Fig. 5a. Theoretically, we observe oscillations in the fraction of atoms on the right of the barrier as the barrier offset is varied. Here, the barrier offset introduces a position shift of the transmitted and reflected wavepackets, which in turn leads to velocity-induced phase gradients across the wavepackets when they recombine. This results in the observed interference fringes. These fringes are modulated by an envelope caused by the changing spatio-temporal overlap between the wavepackets. An approximate analytic model shows that the fringe spacing depends on the soliton velocity and atomic mass m , and that the width of the envelope depends on the soliton length (see Methods). Similar oscillatory behaviour is expected when the transmission of the barrier is varied, as shown in Supplementary Fig. 3. Experimentally, we observe an increased shot-to-shot fluctuation when the barrier is close to the centre of the harmonic potential within an envelope that is in good qualitative agreement with those predicted by quasi-1D and three-dimensional (3D) GPE simulations (see also Supplementary Figs. 4 and 5). In a series of independent measurements (see Methods), we have established that there is a shot-to-shot root mean square (RMS) variation of the axial harmonic potential relative to the barrier position of $1.3\ \mu\text{m}$ in our experiment, illustrated by the green point and horizontal error bar in Fig. 5a. This is comparable to the fringe spacing and means that we are unable to resolve the predicted oscillatory behaviour. It is noteworthy that the theory lines in Fig. 5a have no free fitting parameters and the experimental values for the barrier offset are determined from independent measurements of the trap and barrier positions.

To further elucidate the effects of interference-mediated recombination, we compile histograms of the experimental data in Fig. 5a. The results are shown in Fig. 5b, c for large ($>5\ \mu\text{m}$) and small ($<1.3\ \mu\text{m}$) barrier offsets, respectively. Figure 5d, e show equivalent histograms sampled stochastically from quasi-1D GPE simulations, assuming the experimentally determined $1.3\ \mu\text{m}$ uncertainty in the barrier offset (see Methods). For the large-offset data, we observe a distribution in the measurement of N_R/N_{tot} centred around 0.2 with a width comparable to that obtained for the 50:50 splitting measurement (Fig. 1d). The equivalent theory histogram is also centred on $N_R/N_{\text{tot}} = 0.2$, with a narrower width. We attribute the difference in widths to the imaging noise discussed in context of Fig. 1d, which is not included in the theory. In stark contrast, the histograms for the small-offset data show much greater fluctuation in the population. Again the experimental histogram is broadened due to imaging noise. The increased fluctuation shown in the small-offset histograms is a direct consequence of interference-mediated recombination together with the known and independently characterized shot-to-shot variation in the position of the axial harmonic potential with respect to the barrier.

Discussion

The experimental observations shown in Figs. 4c, d and 5a are definitive signatures of interference-mediated recombination at

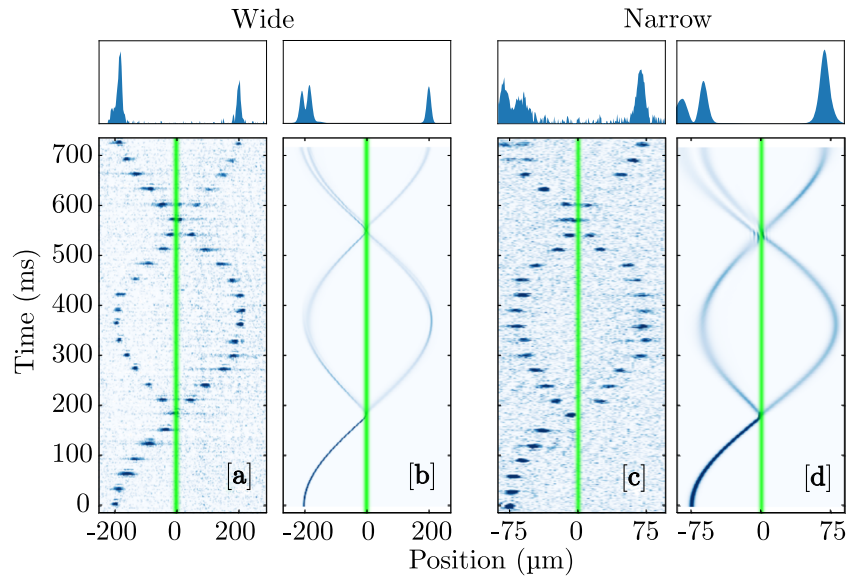


Fig. 4 Trajectories of a soliton with a centred barrier. The soliton undergoes centre of mass oscillations and interacts twice with a barrier centred in the harmonic potential. **a, b** The results for the wide barrier where the soliton kinetic energy per atom at the barrier is $E_k/k_B = 16.0 \pm 0.4$ nK. **a** The experimental image sequence, with the upper panel displaying the signal obtained by integrating across the final image. **b** The results of quasi-1D Gross-Pitaevskii equation (GPE) simulations, with the upper panel displaying the convolution of the final 1D density and the resolution of the imaging system. The barrier is indicated by the green line and the barrier power is held constant throughout each sequence to give a transmission of 0.5 at the first barrier interaction. **c, d** Similar results for the narrow barrier where the soliton kinetic energy per atom at the barrier is $E_k/k_B = 2.2 \pm 0.2$ nK. The experimental images are selected randomly from multiple repeats. For the narrow barrier we observe large shot-to-shot variation following the second barrier interaction.

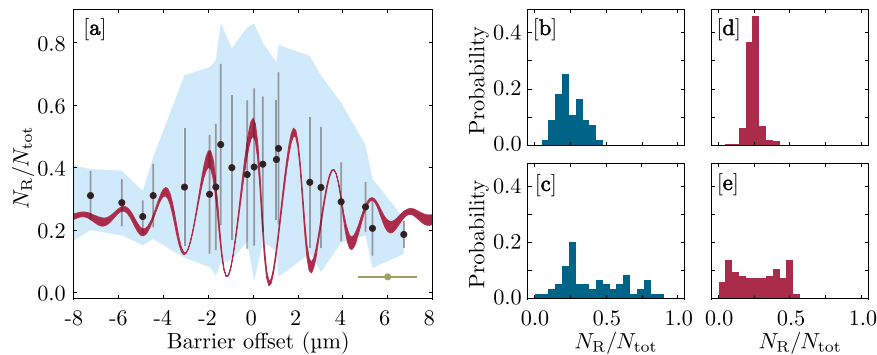


Fig. 5 Sensitivity of the interferometer output to the barrier position. **a** The fraction of atoms on the right of the narrow barrier following the second barrier interaction, as a function of barrier offset. The data points and error bars show the means and SDs across five to ten measurements taken at each offset position. The blue shaded region displays the maximum and minimum values at each offset position. The single green point and horizontal error bar indicate the independently measured shot-to-shot variation in the barrier position. The red oscillatory curve shows the result of a quasi-1D Gross-Pitaevskii equation (GPE) simulation based on experimental parameters, with the thickness reflecting the experimentally determined uncertainty in the barrier width. The kinetic energy of the soliton per atom at the barrier is $E_k/k_B = 2.4 \pm 0.2$ nK. **b, c** Histograms compiled from the experimental data in **a**, for offsets larger than $5 \mu\text{m}$ and less than $1.3 \mu\text{m}$, respectively. These histograms have SDs of 0.086 and 0.22, respectively. **d, e** Equivalent histograms sampled stochastically from quasi-1D GPE simulations, assuming a $1.3 \mu\text{m}$ uncertainty in the barrier offset. They have SDs of 0.041 and 0.16, respectively.

the narrow barrier, as the strong increase in population on the right of the barrier and the increase in population fluctuations can only be explained by interference effects. Without interference, there is no significance to the increased spatio-temporal overlap of the daughter solitons when the barrier is centred, so the same populations and fluctuations would be recovered for all offsets. For the wide barrier, we observe that after the second barrier interaction, although the population on the right increases to $N_R/N_{\text{tot}} \sim 0.25$, the majority of the population still appears on the left with very little fluctuation (see Fig. 4a, b), consistent with the picture that velocity filtering dominates the recombination process. In stark contrast, the histograms in Fig. 5c, e reveal the effect of interference-mediated recombination in the narrow barrier case. We see an additional manifestation of interference in the

double-peak structure on the left of the narrow barrier following the second barrier interaction in Fig. 4c, d, for both theory and experiment; further theoretical simulations demonstrate that introducing an additional phase difference between the daughter solitons can merge the two peaks into one, leaving only a small population on the right of the barrier. This phase dependence is explored theoretically in Supplementary Fig. 6; changes in phase difference between the daughter solitons result in small variations in the final populations for the wide barrier, whereas they result in far more significant variations for the narrow barrier. In principle, if the daughter solitons remain phase coherent from splitting through to recombination, this forms the basis of a phase-sensitive interferometer. However, our independently measured fluctuations in the barrier offset prevent us making

such an interferometer or definitively confirming the phase coherence of the daughter solitons in the current experiment, as explored in Supplementary Fig. 4.

From the theoretical modelling, it is clear that exceptional stability in the relative position between the barrier and axial harmonic potential is required to create a viable interferometer; to resolve the oscillatory behaviour in Fig. 5a requires the barrier to be stable and controllable at the level of $\sim 0.1 \mu\text{m}$ with respect to the harmonic potential. Currently, the axial potential in our experiment is generated magnetically, making it susceptible to uncontrolled stray magnetic fields. Remarkably, a shot-to-shot variation in the ambient magnetic field of only 3 mG is sufficient to fully account for the observed fluctuations, indirectly highlighting the exceptionally high potential sensitivity of a soliton interferometer. This sensitivity to magnetic field could be removed altogether using an all-optical potential generated by, e.g., acousto-optic deflectors^{43,44} or a digital micromirror device⁴⁵. Optical methods are also experimentally attractive, because the shot-to-shot stability of our current optical potentials is $\sim 0.3 \mu\text{m}$ and would probably be sufficient to observe the oscillatory behaviour in Fig. 5a. Furthermore, these methods offer the flexibility for more complicated geometries, such as a ring-shaped trap for a soliton Sagnac interferometer¹⁹. Alternatively, other atomic systems may prove to be more resilient to barrier position. For instance, the lower mass of lithium would result in broader fringes, leading to less-stringent requirements for the relative position stability. The lower mass has the added benefit of making the solitons themselves larger, so the barrier is comparatively narrower and velocity filtering is suppressed.

Our apparatus also lends itself to soliton–soliton collision experiments. As the relative phase of the daughter solitons is expected to be well-defined and controllable, the outcome of soliton–soliton collisions could be controlled completely deterministically, unlike in other reported experiments^{10,11}. The ability to manipulate the daughter solitons' relative velocity and population fractions also allows us to access a wide parameter range of interest^{12,13}. In this context, we highlight the collision between the daughter solitons that occurs around 650 ms for the offset barrier trajectories shown in Fig. 3c, d. We have also observed the daughter solitons to undergo many (>10) soliton–soliton collisions in the absence of the barrier without any instances of mergers or collapse. This is a strong experimental marker for long coherence times.

Our measurements are the first conclusive realization of splitting and interference-mediated recombination of bright matter-wave solitons on a repulsive barrier. We have demonstrated the controlled splitting of a soliton into two daughter solitons, in good agreement with GPE simulations. We have shown that velocity filtering dominates interference during the recombination process for wider barriers, resulting in a merging of the daughter solitons. However, with a reduced barrier width, interference overcomes velocity-filtering effects and interference-mediated recombination is observed through an increased fluctuation in the populations following the second barrier interaction. Our theoretical analysis shows that interference-mediated recombination is extremely sensitive to the barrier position, predicting strong oscillations in the interferometer output as the barrier position is adjusted over just a few micrometres. With this new insight, we are able to attribute the observed population fluctuations to independently measured shot-to-shot variations in the barrier offset due to magnetic field noise. Although our results are completely consistent with coherent splitting and phase-sensitive recombination, a direct measurement of the population oscillations as the barrier offset is varied would provide definitive proof. Our results show that this will require the barrier to be stable and controllable at the level of $\sim 0.1 \mu\text{m}$ with respect to the harmonic potential. This is within reach of future realizations of

the experiment using all-optical potentials that are immune to small variations in the magnetic field, bringing high-sensitivity soliton interferometry closer to reality.

Methods

Soliton production. We create solitons of ~ 2500 ^{85}Rb atoms using methods described in previous publications^{7,36–38}. Briefly, a BEC of up to 7000 ^{85}Rb atoms with a condensate fraction $>80\%$ and temperature $<0.6 T_c$ is formed in a hybrid trap comprising a red-detuned crossed optical dipole trap and a magnetic potential provided by quadupole and bias fields. The s -wave scattering length is set to $\sim 220 a_0$ by tuning the magnetic field near the 165.75 G zero crossing of a broad magnetic Feshbach resonance in the $F=2$, $m_F=-2$ state^{46–48}. To form a soliton, the scattering length is first ramped to zero over 100 ms before simultaneously removing one dipole trapping beam and jumping the scattering length to a small negative value. Stable solitons are formed in the resulting waveguide for scattering lengths in the range of $-13.5 a_0 \lesssim a_s \lesssim -7 a_0$, with soliton production possible up to approximately $-20 a_0$ for a reduced number of atoms.

An additional pair of magnetic coils produces a harmonic confining potential in the axial direction of the waveguide, with trapping frequencies of up to $\omega_z/2\pi \sim 1.5$ Hz, allowing us to observe axial centre-of-mass oscillations of the soliton along the waveguide. The centre of the harmonic potential is maneuvered along the axial direction using a pair of “shim” coils, which, coupled with independent control over the barrier position, provides control of the soliton velocity at the barrier. As the harmonic potential is magnetic, the soliton experiences a changing magnetic field as it oscillates. However, the field varies by <1 mG across a typical centre of mass oscillation. This has a negligible effect on the scattering length ($<0.1 a_0$ at $a_s = -10a_0$) and so does not affect the stability of the soliton.

Soliton beam splitter. The light for the Gaussian barrier is produced by a 532 nm laser. A cylindrical lens forms a highly elliptical beam, which is focussed onto the waveguide such that the narrow axis is oriented along the axial direction of the trap. The barrier potential height is controlled by changing the beam power and the barrier position along the waveguide can be precisely adjusted via a piezo-actuated mirror. The two barrier widths investigated in this work are generated using two different objective lenses, with focal lengths of 100 mm and 30 mm for the wide and narrow barriers, respectively.

To characterize the width of the narrow barrier, the beam is exposed onto an elongated cloud of thermal atoms and the resultant dip in atomic density observed in the images is fitted using a Gaussian profile (see Supplementary Fig. 7). Using this technique, we measure a width along the waveguide axial direction of $w_z = 4.7 \pm 0.3 \mu\text{m}$, which, when corrected for the $3.0 \pm 0.3 \mu\text{m}$ resolution limit of the imaging system (see below), becomes $3.6 \pm 0.4 \mu\text{m}$. By translating the thermal cloud across the barrier beam, we also determine the transverse width to be $w_x = 117 \pm 9 \mu\text{m}$ in the plane of the atoms.

To determine the width of the wide barrier, the beam is profiled outside of the vacuum chamber using a duplicate optical setup. Using this method, we measure an axial waist of $w_z = 10.6^{+0.5}_{-0.1} \mu\text{m}$ and a transverse width at the axial waist position of $w_x = 434 \pm 5 \mu\text{m}$. The asymmetry in uncertainty for w_z accounts for uncertainties in the position of the focus inside the vacuum chamber, which can only lead to a larger barrier width.

Quasi-1D GPE theory is also fitted to splitting data with the barrier width in the axial direction of the waveguide as the only free parameter (as in Fig. 1b) for both the narrow and wide barriers. The transverse barrier widths are constrained by the experimental values above. Using this technique, we determine barrier widths of $w_z = 4.8 \pm 0.2 \mu\text{m}$ and $w_z = 11.9 \pm 0.3 \mu\text{m}$ for the narrow and wide barrier beams, respectively. The uncertainty in each value is the standard error in the fitted widths across several sets of splitting data, taken for various soliton velocities. Any assumptions of the quasi-1D GPE model that are not fulfilled in the experiment (e.g., in the transverse mode profiles) could contribute to the small discrepancy with the measured values.

Imaging. We perform in-situ, high-field, high-intensity absorption imaging of the solitons. Imaging at high field ensures that the soliton wavepackets are not perturbed by crossing the Feshbach resonance during trap turn-off, which broadens their shape significantly. Intense, short probe pulses are used to minimize width broadening as a result of photon recoil^{49,50}.

At a magnetic field of ~ 165.85 G, where experiments are performed, there are no closed optical transitions from the $F=2$, $m_F=-2$ ground state. This is detrimental to imaging, as each atom can only scatter an average of 3.28 photons before being lost to a dark state. We circumvent this by transferring atoms from $F=2$, $m_F=-2$ to $F=3$, $m_F=-3$ via microwave adiabatic rapid passage (ARP), from which a closed σ^+ transition exists. A typical imaging sequence begins with a 100 μs , 300 kHz ARP sweep to transfer $\sim 90\%$ of the atoms to the imaging state, followed by a 10 μs probe pulse with an intensity of $\sim 10 I_{\text{sat}}$.

The resolution limit of the imaging system is expected to be of the order of the soliton width for the 30 mm objective lens system. The observed soliton in the image plane is the convolution of the soliton in the object plane with the point spread function of the imaging system. As the width of a soliton doubles when the atom number is halved, for a constant interaction strength, we can estimate the

resolution limit of the imaging system by imaging the soliton before and after splitting, with the barrier set to 50% transmission. In this case, we find that the resolution limit r is given by

$$r = \sqrt{\frac{4k_N^2 - k_{N/2}^2}{3}}, \quad (1)$$

where k_N and $k_{N/2}$ are the measured widths before and after splitting, respectively. Over ten experimental runs each, we measure an average soliton width of $3.6 \pm 0.2 \mu\text{m}$ and average width of the daughter solitons of $4.9 \pm 0.3 \mu\text{m}$, where the quoted uncertainty represents the standard error across the runs. This implies a resolution limit of $3.0 \pm 0.3 \mu\text{m}$, in good agreement with the diffraction-limited value of $2.9 \mu\text{m}$ for our optical system. By removing the effects of the resolution limit, we calculate the true observed soliton width to be $2.0 \pm 0.5 \mu\text{m}$, which is in excellent agreement with the $1.8 \mu\text{m}$ predicted from GPE theory.

To account for the resolution limit in the GPE simulations, a $3 \mu\text{m}$ Gaussian convolution is applied to the quasi-1D GPE density profiles in Figs. 3d and 4d. As both the initial and daughter soliton widths are below the resolution limit for the 100 mm lens, it is impossible to accurately apply Eq. (1). Instead, the resolution limit is extrapolated from the measured 30 mm lens resolution using the ratio of the focal lengths of the two objective lenses. Therefore, a $10 \mu\text{m}$ Gaussian convolution is applied to the quasi-1D GPE density profiles in Figs. 3b and 4b.

The change of objective lens also alters the camera's field of view. Therefore, it was necessary to reduce the centre of mass oscillation amplitude in Figs. 3c and 4c ($75 \mu\text{m}$) from that in Figs. 3a and 4a ($225 \mu\text{m}$) to compensate.

Trap stability. We determine the RMS shot-to-shot fluctuation in the position of the centre of the axial potential to set the offset uncertainty in Fig. 5a. This is found by taking ten repeat measurements of the soliton position both immediately after release and after half a trap period, finding shot-to-shot variations of $0.3 \pm 0.1 \mu\text{m}$ and $2.6 \pm 0.6 \mu\text{m}$, respectively. These variations imply fluctuations in the position of the centre of the harmonic potential of $1.3 \pm 0.3 \mu\text{m}$. This is comparable to the fringe period in Fig. 5a predicted by GPE simulations, meaning that the experiment samples some region of the fringes on each run; hence, the increased variation when the barrier is close to the centre of the harmonic potential. As the uncertainty is dominated by position fluctuations after a half trapping period, we attribute it to be dominated by magnetic potential instability. A stray field of only $\sim 3.0 \text{ mG}$ along the axial direction would account for this shot-to-shot fluctuation. From another set of ten sequences, we determine the barrier position to fluctuate from shot-to-shot with an RMS of $0.3 \pm 0.1 \mu\text{m}$. This is small enough to resolve the fringes in Fig. 5a, for a similarly stable harmonic potential.

Gross-Pitaevskii model. Assuming a mean-field description, the collective wavefunction ψ (normalized to unity) obeys the GPE

$$i\hbar \frac{\partial \psi}{\partial t} = \left[\frac{-\hbar^2}{2m} \nabla^2 + \frac{m[\omega_z^2 z^2 + \omega_r^2(x^2 + y^2)]}{2} + \mathcal{V}(x, z) + g_{3D} |\psi|^2 \right] \psi, \quad (2)$$

where m is the atomic mass, ω_z is the axial trap frequency, ω_r is the radial trap frequency, $g_{3D} = 4\pi\hbar^2 N a_s / m$ where a_s is the s -wave scattering length and N is the atom number. The optical barrier potential is modelled as $\mathcal{V}(x, z) = U(x)V(z)$, with

$$U(x) = \exp\left[\frac{-2x^2}{w_x^2}\right], \quad (3)$$

$$V(z) = \frac{\alpha P}{\epsilon_0 c \pi w_x w_x} \exp\left[\frac{-2(z - z_{\text{off}})^2}{w_z^2}\right], \quad (4)$$

where α is the relevant polarizability for ^{85}Rb , z_{off} is the barrier offset from the centre of the trap and P is the optical power in the beam.

As $\omega_r \gg \omega_z$, we also investigate a simpler quasi-1D model by assuming the atoms to be frozen in the ground state of the radial oscillator potential, resulting in effective quasi-1D GPE

$$i\hbar \frac{\partial \psi}{\partial t} = \left[\frac{-\hbar^2}{2m} \frac{\partial^2}{\partial z^2} + \frac{m\omega_z^2 z^2}{2} + V(z) + g_{1D} |\psi|^2 \right] \psi, \quad (5)$$

with effective interaction strength

$$g_{1D} = 2\hbar\omega_r a_s N. \quad (6)$$

In all simulations, we take $a_s = -10 a_0$ (where a_0 is the Bohr radius), $\omega_r = 2\pi \times 40 \text{ Hz}$ and $\omega_z = 2\pi \times 1.4 \text{ Hz}$. We generally take $w_x = 117 \mu\text{m}$, although simulations for the wide barrier (Figs. 1b, 3b and 4b) have $w_x = 434 \mu\text{m}$. We take $N = 2500$ in quasi-1D ($N = 2000$ in 3D). We assume the initial condition to be a soliton in its ground state with respect to the waveguide potential, displaced to position $-z_0$. The parameters w_x , z_{off} and z_0 are varied as described elsewhere. Our numerical simulations all use Fourier pseudospectral methods and a fourth- to fifth-order adaptive Runge-Kutta scheme to obtain the real-time evolution. Our 3D simulations run on graphics processing units and obtain ground states using imaginary time evolution. Our quasi-1D simulations obtain ground states using an iterative biconjugate gradient scheme.

Stochastic sampling of the quasi-1D Gross-Pitaevskii results. We produce the theoretical histograms shown in Fig. 5d, e and curves shown in Supplementary Fig. 4 by a stochastic sampling method. We first simulate the splitting and recombination process using the quasi-1D GPE as described above, with $w_x = 3.6 \mu\text{m}$, for a range of 961 equally spaced barrier offsets $-12 \mu\text{m} \leq z_{\text{off}} \leq 12 \mu\text{m}$. We repeat these simulations with an artificially imposed phase shift ϕ of one of the daughter solitons following splitting, but prior to recombination, for 50 equally spaced phase shifts $0 \leq \phi < 2\pi$. These simulations yield 48,050 samples of the transmitted fraction $N_R/N_{\text{tot}} \equiv A$ as a function of z_{off} and ϕ , from which we construct a bivariate cubic spline interpolant of the function $A(z_{\text{off}}, \phi)$.

To construct the histograms in Fig. 5d, e, we assume the actual barrier offsets z_{off} for every experimental run contributing to the data shown in Fig. 5a can be expected to vary as a Gaussian distribution about the experimentally measured value \bar{z}_{off} with SD equal to the measured $1.3 \mu\text{m}$ barrier offset uncertainty. For each experimental run, we sample 10^4 values of z_{off} from this distribution and use the interpolant described above to find $A(z_{\text{off}}, 0)$ in each case. Figure 5d, e show, respectively, the normalized histograms of the $A(z_{\text{off}}, 0)$ values obtained if we select only data from experimental runs with experimentally measured $z_{\text{off}} > 5 \mu\text{m}$ and $z_{\text{off}} < 1.3 \mu\text{m}$. The same technique is used to construct the mean and SD of the distribution of $A(z_{\text{off}}, 0)$ as a function of the experimentally measured barrier offset \bar{z}_{off} shown in Supplementary Fig. 4.

We also explore the distribution of sampled values of $A(z_{\text{off}}, \phi)$ if z_{off} is held fixed and a phase shift ϕ chosen randomly between 0 and 2π is imposed on one of the daughter solitons before recombination (again, A is sampled from the interpolant described above). The effects of adding this phase noise are shown in Supplementary Fig. 4.

Finally, we have performed some simulations to estimate possible thermal effects beyond the GPE description. This is complicated by the fact that in the experiment solitons are produced and released into the waveguide in a non-equilibrium, three-dimensional process; modelling this directly with a 3D beyond-mean-field description is not feasible. We obtain a rough worst-case estimate using a quasi-1D classical field approach. First, we assume a condensate thermalized at 20 nK in the crossed dipole trap (assumed to have isotropic trap frequency 40 Hz) at $a_s = 0$. In addition to a condensate of 2500 atoms in the oscillator ground state, we populate the excited oscillator modes with complex Gaussian stochastic noise such that the average occupation of each mode matches a Bose-Einstein distribution at 20 nK . To obtain a quasi-1D description, we sum the amplitudes over all modes in the x and y directions, obtaining an ensemble of quasi-1D wavefunctions with on average ≈ 4000 atoms that can be evolved in the quasi-1D GPE. We evolve an ensemble of 200 such stochastic wavefunctions through the collision process for the narrow barrier with $z_0 = 75 \mu\text{m}$, $z_{\text{off}} = 0$, and with a barrier power chosen to obtain average transmission ≈ 0.5 . Extending these ensemble simulations to other barrier offsets produces a distribution qualitatively similar to the distribution obtained when adding phase noise as described above and shown in Supplementary Fig. 4. However, we find the SD of the initial splitting computed over the ensemble with $z_{\text{off}} = 0$ to be 0.047 . The experimentally measured SD of this quantity for the narrow barrier in Fig. 1a is 0.064 , which, as described in the study, we expect to contain a significant contribution from imaging noise. That we do not measure a higher SD in the experiment suggests that these simulations overestimate thermal effects. However, improved barrier stability would be needed to accurately measure the actual thermal effects in the experiment.

Approximate analytic quasi-1D model. To understand the nature of recombination, particularly the appearance of interference fringes as z_{off} is varied, we outline a simple approximate analytic model for the fraction of the atoms found on the "right" of the barrier ($z > z_{\text{off}}$) following the second barrier interaction. For convenience, we denote this quantity $A \equiv N_R/N_{\text{tot}}$ and our analytic estimate of it A_{est} . It is convenient to develop the following in dimensionless "soliton" units defined by length $\ell_s = \hbar/(2m\omega_r a_s |N|)$, time $t_s = \hbar/(4m\omega_z^2 |a_s|^2 N^2)$ and energy $E_s = 4m\omega_r^2 |a_s|^2 N^2$. In these units, the quasi-1D GPE becomes

$$i \frac{\partial \tilde{\psi}}{\partial t} = \left[-\frac{1}{2} \frac{\partial^2}{\partial \tilde{z}^2} + \frac{E_s^2 \tilde{z}^2}{2E_s^2} + \frac{\tilde{q}}{\tilde{\ell}} \sqrt{\frac{2}{\pi}} \exp\left(\frac{-2(\tilde{z} - \tilde{z}_{\text{off}})^2}{\tilde{\ell}^2}\right) - |\tilde{\psi}|^2 \right] \tilde{\psi}, \quad (7)$$

where $\tilde{\ell} = w_x/\ell_s$ and

$$\tilde{q} = \frac{\alpha P}{2\sqrt{2}\pi\hbar\epsilon_0 c w_x \omega_r |a_s| N}. \quad (8)$$

Dimensionless velocities are given by

$$\tilde{v} = \frac{v}{2\omega_r |a_s| N}. \quad (9)$$

Ignoring the relative phase of the solitons, the timing of the various barrier interactions, the interatomic interactions and assuming the waveguide potential to be constant over the width of the barrier, A_{est} can be approximated by using the known result for scattering from a sech-squared potential⁴¹. Specifically, approximating the optical barrier potential by

$$V(z) = \frac{\tilde{q}}{\tilde{\ell}} \sqrt{\frac{2}{\pi}} \exp\left(\frac{-2(\tilde{z} - \tilde{z}_{\text{off}})^2}{\tilde{\ell}^2}\right) \approx \frac{\tilde{q}}{\tilde{\ell}} \sqrt{\frac{2}{\pi}} \text{sech}^2\left(\frac{\pi(\tilde{z} - \tilde{z}_{\text{off}})}{\kappa\tilde{\ell}}\right), \quad (10)$$

where $\kappa = (\pi/2)^{3/2}$, we obtain the approximate transmission probability for a single barrier interaction

$$T(\bar{v}) = \frac{\sinh^2(\kappa\bar{v})}{\sinh^2(\kappa\bar{v}) + \cosh^2\left(\frac{\pi}{2}\sqrt{4\kappa\bar{q}\bar{\ell}/\pi - 1}\right)}. \quad (11)$$

We assume that the atoms impact the barrier at the first interaction in the form of an ideal soliton with dimensionless velocity $\bar{v}_{\text{in}} = z_0\omega_z/(2\omega_r|a_s|N)$, chosen such that in the quasi-1D numerics the transmitted fraction is 1/2. The velocity \bar{v}_{half} at which $T(\bar{v}_{\text{half}}) = 1/2$ is typically very close to this. After the first barrier interaction, the amplitudes of the outgoing wavepackets in momentum space are approximately

$$|\bar{\psi}_{z>z_{\text{off}}}(\bar{v})| \approx t(\bar{v} - \bar{v}_{\text{in}} + \bar{v}_{\text{half}})\text{sech}[\pi(\bar{v} - \bar{v}_{\text{in}})]\sqrt{\pi/2}, \quad (12)$$

$$|\bar{\psi}_{z<z_{\text{off}}}(\bar{v})| \approx r(\bar{v} - \bar{v}_{\text{in}} + \bar{v}_{\text{half}})\text{sech}[\pi(\bar{v} - \bar{v}_{\text{in}})]\sqrt{\pi/2}, \quad (13)$$

where $t(\bar{v}) = T(\bar{v})^{1/2}$ and $r(\bar{v}) = [1 - T(\bar{v})]^{1/2}$. Between the first and second barrier interactions the wavepackets undergo nonlinear evolution. We empirically approximate this by assuming that the wavepackets re-form into solitons with half of the initial amplitude, preserving the location in momentum space of the peak of the transmitted or reflected amplitude, as obtained from Eqs. (12)–(13). This gives wavepackets incoming to the second barrier interaction

$$\bar{\psi}'_{z>z_{\text{off}}}(\bar{v}) \approx \text{sech}[2\pi(\bar{v} - \bar{v}_{t,\text{peak}})]\sqrt{\pi/2}, \quad (14)$$

$$\bar{\psi}'_{z<z_{\text{off}}}(\bar{v}) \approx \text{sech}[2\pi(\bar{v} - \bar{v}_{r,\text{peak}})]\sqrt{\pi/2}, \quad (15)$$

where $\bar{v}_{t,\text{peak}}$ and $\bar{v}_{r,\text{peak}}$ denote the numerically determined locations of the peaks described. Finally, the fraction of the total population to the right is approximated by

$$A_{\text{est}}^{(0)} = \int \left| t(\bar{v} - \bar{v}_{\text{in}} + \bar{v}_{\text{half}})\bar{\psi}'_{z>z_{\text{off}}}(\bar{v}) + r(\bar{v} - \bar{v}_{\text{in}} + \bar{v}_{\text{half}})\bar{\psi}'_{z<z_{\text{off}}}(\bar{v}) \right|^2 d\bar{v}. \quad (16)$$

The estimate above will be modulated by interference between the solitons. We model this using the approach for δ -function barriers described in ref. 21. This is expected to be a good approximation for narrow barriers when the dimensionless soliton velocity at the barrier $\bar{v}_{\text{in}} \gtrsim 1$. Assuming $z_0 \gg z_{\text{off}}$ the dimensionless velocity of all solitons is $\sim \pm \bar{v}_{\text{in}}$ when they are in the neighbourhood of the barrier. In this approximation, the two solitons to the right of the barrier are separated by $4z_{\text{off}}$. Thus, the wavefunction to the right ($z > z_{\text{off}}$) immediately after recombination can be written as

$$\bar{\psi}_{\text{right}}(\bar{z}) \approx \frac{\sqrt{A_{\text{est}}^{(0)}}}{4} \left[e^{i\bar{v}_{\text{in}}\bar{z}} \text{sech}\left(\frac{\bar{z} - \bar{v}_{\text{in}}\bar{t}}{4}\right) + e^{i\bar{v}_{\text{in}}(\bar{z} - 4z_{\text{off}})} \text{sech}\left(\frac{\bar{z} - 4z_{\text{off}} - \bar{v}_{\text{in}}\bar{t}}{4}\right) \right], \quad (17)$$

where we have assumed equal-amplitude solitons. It is noteworthy that we have omitted numerous irrelevant phase factors compared to the expressions in ref. 21 for simplicity, and the phase shift of $\pi/2$ gained by the soliton transmitted at the second barrier interaction simply cancels the phase that the soliton reflected at the second barrier interaction previously acquired by being transmitted at the first barrier interaction. Integrating $|\bar{\psi}_{\text{right}}(\bar{z})|^2$, we obtain

$$A_{\text{est}} = A_{\text{est}}^{(0)} \left[1 + \cos(4\bar{v}_{\text{in}}\bar{z}_{\text{off}}) \frac{\bar{z}_{\text{off}}}{\sinh(\bar{z}_{\text{off}})} \right] = A_{\text{est}}^{(0)} \left[1 + \cos\left(\frac{4z_0 z_{\text{off}}}{\ell_0^2}\right) \frac{z_{\text{off}}/\ell_s}{\sinh(z_{\text{off}}/\ell_s)} \right], \quad (18)$$

where the final expression is in real units, the velocity v_{in} has been replaced with $z_0\omega_z$, and $\ell_0 = (\hbar/m\omega_z)^{1/2}$ is the axial harmonic oscillator length.

As shown in the Supplementary Figs. 8 and 9, the analytic approximation gives a good qualitative picture of the behaviour across a wide regime of parameters and provides a quantitatively accurate value for the fringe spacing across a considerable fraction of this. In particular, we find it can give useful results for barrier interactions with $\bar{v}_{\text{in}} \lesssim 1$. However, it does break down for wider barriers and slower barrier interactions.

Data availability

The data presented in this article are available at <https://doi.org/10.15128/r1sf2685090>.

Received: 31 January 2020; Accepted: 20 February 2020;

Published online: 13 March 2020

References

- Kivshar, Y. S. & Malomed, B. A. Dynamics of solitons in nearly integrable systems. *Rev. Mod. Phys.* **61**, 763–915 (1989).
- Kartashov, Y. V., Malomed, B. A. & Torner, L. Solitons in nonlinear lattices. *Rev. Mod. Phys.* **83**, 247–305 (2011).

- Chin, C., Grimm, R., Julienne, P. & Tiesinga, E. Feshbach resonances in ultracold gases. *Rev. Mod. Phys.* **82**, 1225–1286 (2010).
- Strecker, K. E., Partridge, G. B., Truscott, A. G. & Hulet, R. G. Formation and propagation of matter-wave soliton trains. *Nature* **417**, 150 (2002).
- Khaykovich, L. et al. Formation of a matter-wave bright soliton. *Science* **296**, 1290–1293 (2002).
- Cornish, S. L., Thompson, S. T. & Wieman, C. E. Formation of bright matter-wave solitons during the collapse of attractive Bose-Einstein condensates. *Phys. Rev. Lett.* **96**, 170401 (2006).
- Marchant, A. L. et al. Controlled formation and reflection of a bright solitary matter-wave. *Nat. Commun.* **4**, 1865 (2013).
- McDonald, G. D. et al. Bright solitonic matter-wave interferometer. *Phys. Rev. Lett.* **113**, 013002 (2014).
- Lepoutre, S. et al. Production of strongly bound ^{39}K bright solitons. *Phys. Rev. A* **94**, 053626 (2016).
- Mežnaršič, T. et al. Cesium bright matter-wave solitons and soliton trains. *Phys. Rev. A* **99**, 033625 (2019).
- Nguyen, J. H., Dyke, P., Luo, D., Malomed, B. A. & Hulet, R. G. Collisions of matter-wave solitons. *Nat. Physics* **10**, 918 (2014).
- Parker, N. G., Martin, A. M., Cornish, S. L. & Adams, C. S. Collisions of bright solitary matter waves. *J. Phys. B At. Mol. Opt. Phys.* **41**, 045303 (2008).
- Billam, T. P., Cornish, S. L. & Gardiner, S. A. Realizing bright-matter-wave-soliton collisions with controlled relative phase. *Phys. Rev. A* **83**, 041602 (2011).
- Choudhury, S., Sreedharan, A., Mukherjee, R., Streltsov, A. & Wüster, S. Condensate soliton collisions beyond mean-field theory. Preprint at arXiv:1904.11878 <https://journals.aps.org/pr/accepted/d907bn80R7b17c1717f0985635b44e4f81da4d5ee> (2019).
- Martin, A. D. & Ruostekoski, J. Quantum dynamics of atomic bright solitons under splitting and recollision, and implications for interferometry. *New J. Phys.* **14**, 043040 (2012).
- Sakaguchi, H. & Malomed, B. A. Matter-wave soliton interferometer based on a nonlinear splitter. *New J. Phys.* **18**, 025020 (2016).
- Abdullaev, F. K. & Brazhnyi, V. A. Solitons in dipolar Bose-Einstein condensates with a trap and barrier potential. *J. Phys. B* **45**, 085301 (2012).
- Polo, J. & Ahufinger, V. Soliton-based matter-wave interferometer. *Phys. Rev. A* **88**, 053628 (2013).
- Helm, J. L., Cornish, S. L. & Gardiner, S. A. Sagnac interferometry using bright matter-wave solitons. *Phys. Rev. Lett.* **114**, 134101 (2015).
- Helm, J. L., Rooney, S. J., Weiss, C. & Gardiner, S. A. Splitting bright matter-wave solitons on narrow potential barriers: quantum to classical transition and applications to interferometry. *Phys. Rev. A* **89**, 033610 (2014).
- Helm, J. L., Billam, T. P. & Gardiner, S. A. Bright matter-wave soliton collisions at narrow barriers. *Phys. Rev. A* **85**, 053621 (2012).
- Cuevas, J., Kevrekidis, P. G., Malomed, B. A., Dyke, P. & Hulet, R. G. Interactions of solitons with a gaussian barrier: splitting and recombination in quasi-one-dimensional and three-dimensional settings. *New J. Phys.* **15**, 063006 (2013).
- Cronin, A. D., Schmiedmayer, J. & Pritchard, D. E. Optics and interferometry with atoms and molecules. *Rev. Mod. Phys.* **81**, 1051–1129 (2009).
- Adams, C. S., Sigel, M. & Mlynek, J. Atom optics. *Phys. Rep.* **240**, 143–210 (1994).
- Godun, R., D’Arcy, M., Summy, G. & Burnett, K. Prospects for atom interferometry. *Contemp. Phys.* **42**, 77–95 (2001).
- Pritchard, D., Cronin, A. D., Gupta, S. & Kokořowski, D. Atom optics: Old ideas, current technology, and new results. *Annal. Phys.* **10**, 35–54 (2001).
- Berrada, T. et al. Integrated Mach-Zehnder interferometer for Bose-Einstein condensates. *Nat. Commun.* **4**, 2077 (2013).
- Fattori, M. et al. Atom interferometry with a weakly interacting Bose-Einstein condensate. *Phys. Rev. Lett.* **100**, 080405 (2008).
- Gustavsson, M. et al. Control of interaction-induced dephasing of Bloch oscillations. *Phys. Rev. Lett.* **100**, 080404 (2008).
- Kitagawa, M. & Ueda, M. Squeezed spin states. *Phys. Rev. A* **47**, 5138–5143 (1993).
- Jo, G.-B. et al. Long phase coherence time and number squeezing of two Bose-Einstein condensates on an atom chip. *Phys. Rev. Lett.* **98**, 030407 (2007).
- Haine, S. A. Quantum noise in bright soliton matterwave interferometry. *New J. Phys.* **20**, 033009 (2018).
- Manju, P. et al. Quantum tunneling dynamics of an interacting Bose-Einstein condensate through a gaussian barrier. *Phys. Rev. A* **98**, 053629 (2018).
- Sun, Z.-Y., Kevrekidis, P. G. & Krüger, P. Mean-field analog of the Hong-Ou-Mandel experiment with bright solitons. *Phys. Rev. A* **90**, 063612 (2014).
- Holmer, J., Marzuola, J. & Zworski, M. Fast soliton scattering by delta impurities. *Commun. Math. Phys.* **274**, 187–216 (2007).
- Händel, S., Marchant, A. L., Wiles, T. P., Hopkins, S. A. & Cornish, S. L. Magnetic transport apparatus for the production of ultracold atomic gases in the vicinity of a dielectric surface. *Rev. Sci. Instrum.* **83**, 013105 (2012).
- Marchant, A. L. et al. Quantum reflection of bright solitary matter waves from a narrow attractive potential. *Phys. Rev. A* **93**, 021604 (2016).

38. Marchant, A. L., Händel, S., Hopkins, S. A., Wiles, T. P. & Cornish, S. L. Bose-Einstein condensation of ^{85}Rb by direct evaporation in an optical dipole trap. *Phys. Rev. A* **85**, 053647 (2012).
39. Weiss, C. & Castin, Y. Creation and detection of a mesoscopic gas in a nonlocal quantum superposition. *Phys. Rev. Lett.* **102**, 010403 (2009).
40. Streltsov, A. I., Alon, O. E. & Cederbaum, L. S. Scattering of an attractive Bose-Einstein condensate from a barrier: formation of quantum superposition states. *Phys. Rev. A* **80**, 043616 (2009).
41. Landau, L. & Lifshitz, E. *Quantum Mechanics: Non-Relativistic Theory. Course of Theoretical Physics* (Elsevier Science, 1981).
42. Molony, P. K. et al. Creation of ultracold $^{87}\text{Rb}^{133}\text{Cs}$ molecules in the rovibrational ground state. *Phys. Rev. Lett.* **113**, 255301 (2014).
43. Henderson, K., Ryu, C., MacCormick, C. & Boshier, M. Experimental demonstration of painting arbitrary and dynamic potentials for Bose-Einstein condensates. *New J. Phys.* **11**, 043030 (2009).
44. Schnelle, S., Van Ooijen, E., Davis, M., Heckenberg, N. & Rubinsztein-Dunlop, H. Versatile two-dimensional potentials for ultra-cold atoms. *Opt. Express* **16**, 1405–1412 (2008).
45. Gauthier, G. et al. Direct imaging of a digital-micromirror device for configurable microscopic optical potentials. *Optica* **3**, 1136–1143 (2016).
46. Blackley, C. L. et al. Feshbach resonances in ultracold ^{85}Rb . *Phys. Rev. A* **87**, 033611 (2013).
47. Roberts, J. L. et al. Resonant magnetic field control of elastic scattering in cold ^{85}Rb . *Phys. Rev. Lett.* **81**, 5109–5112 (1998).
48. Claussen, N. R. et al. Very-high-precision bound-state spectroscopy near a ^{85}Rb Feshbach resonance. *Phys. Rev. A* **67**, 060701 (2003).
49. Hueck, K. et al. Calibrating high intensity absorption imaging of ultracold atoms. *Opt. Express* **25**, 8670–8679 (2017).
50. Reinaudi, G., Lahaye, T., Wang, Z. & Guéry-Odelin, D. Strong saturation absorption imaging of dense clouds of ultracold atoms. *Opt. Lett.* **32**, 3143–3145 (2007).

Acknowledgements

This research made use of the Rocket High Performance Computing service at Newcastle University. We acknowledge the UK Engineering and Physical Sciences Research Council (Grants No. EP/L010844/1 and No. EP/K030558/1) for funding.

Author contributions

O.J.W. and A.R. performed the experiments and O.J.W. analysed the data. T.P.B. performed the 1D-GPE simulations and J.L.H. performed the 3D-GPE simulations. S.A.G. contributed to the theoretical interpretation and S.L.C. was involved with all aspects of the experiment. All authors discussed the experimental results, theoretical interpretation and implications. All authors took part in preparing the manuscript.

Competing interests

The authors declare no competing interests.

Additional information

Supplementary information is available for this paper at <https://doi.org/10.1038/s42005-020-0320-8>.

Correspondence and requests for materials should be addressed to S.L.C.

Reprints and permission information is available at <http://www.nature.com/reprints>

Publisher's note Springer Nature remains neutral with regard to jurisdictional claims in published maps and institutional affiliations.



Open Access This article is licensed under a Creative Commons Attribution 4.0 International License, which permits use, sharing, adaptation, distribution and reproduction in any medium or format, as long as you give appropriate credit to the original author(s) and the source, provide a link to the Creative Commons license, and indicate if changes were made. The images or other third party material in this article are included in the article's Creative Commons license, unless indicated otherwise in a credit line to the material. If material is not included in the article's Creative Commons license and your intended use is not permitted by statutory regulation or exceeds the permitted use, you will need to obtain permission directly from the copyright holder. To view a copy of this license, visit <http://creativecommons.org/licenses/by/4.0/>.

© The Author(s) 2020